Accepted Manuscript

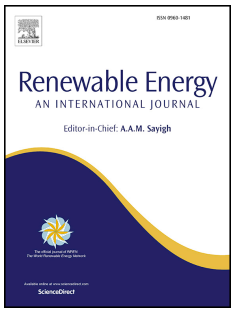

Stability and photo-thermal conversion performance of binary nanofluids for solar absorption refrigeration systems

E. Nourafkan, M. Asachi, H. Jin, D. Wen, W. Ahmed

PII: S0960-1481(19)30094-1

DOI: https://doi.org/10.1016/j.renene.2019.01.081

Reference: RENE 11082

To appear in: *Renewable Energy*

Received Date: 8 November 2018

Revised Date: 12 January 2019

Accepted Date: 22 January 2019

Please cite this article as: Nourafkan E, Asachi M, Jin H, Wen D, Ahmed W, Stability and photo-thermal conversion performance of binary nanofluids for solar absorption refrigeration systems, *Renewable Energy* (2019), doi: https://doi.org/10.1016/j.renene.2019.01.081.

Graphical abstract

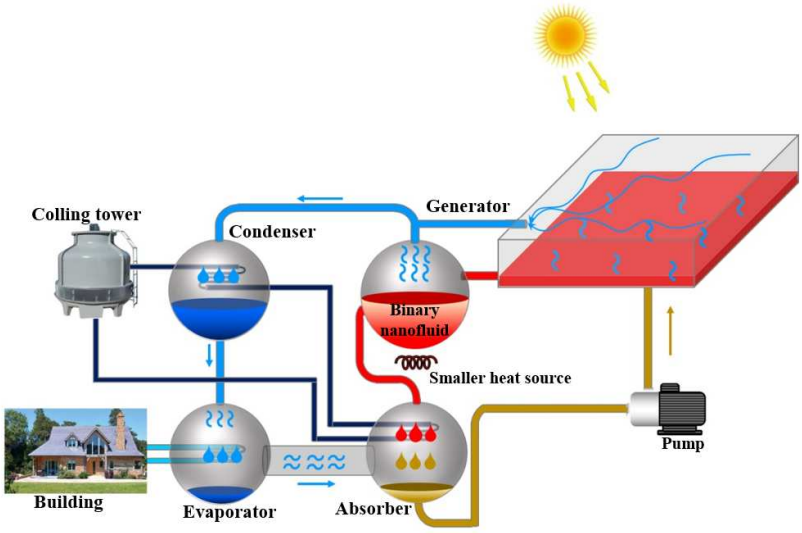

Stability and Photo-Thermal Conversion Performance of Binary Nanofluids for Solar Absorption Refrigeration Systems

E. Nourafkan[1,2*], M. Asachi[2], H. Jin[3], D. Wen[2,3], W. Ahmed[1]

[1]School of Mathematics and Physics, University of Lincoln, Lincoln, LN6 7TS, U.K.

[2]School of Chemical and Process Engineering, University of Leeds, Leeds, LS2 9JT, U.K.

[3]School of Aeronautic Science and Engineering, Beihang University, China.

ABSTRACT

The photo-thermal conversion characteristics of a long-term stable binary nanofluid (nanoparticles in 50 wt% lithium bromide-50 wt% water) were investigated in this work. The stability of the binary nanofluid against the agglomeration and sedimentation process was evaluated by a high-speed centrifuge analyzer and transmission electron microscopy. The photo-thermal conversion efficiency of the nanofluid was also studied using a solar simulator. Experimental results indicated that the use of the binary nanofluid could significantly increase the light trapping efficiency and, therefore, the bulk temperature, which in turn could increase the evaporation rate due to surface localized heat generation. The experimental results showed the increase of 4.2 and 4.9 percent solar radiative energy in the form of sensible heat after addition of 64 and 321 mg/l iron oxide NPs to the pure water, respectively. The increasing percent is 4.9% and 11.9% for latent heat efficiency in the presence of 64 and 321 mg/l iron oxide NPs, respectively. Possessing both high stability and excellent photo-thermal conversion rate, rod shape iron oxide nanoparticles is suggested to be a potential candidate used for the solar absorption refrigeration systems.

Keywords: Log-term Stable Binary Nanofluid, Lithium Bromide, Solar Absorption Refrigeration System, Photo-Thermal Conversion.

1. Introduction

Corresponding author: Dr. Ehsan Nourafkan (Enourafkan@lincoln.ac.uk, e.nourafkan@leeds.ac.uk)

Utilizing solar light as a green energy to run the air conditioning systems is a promising technique to replace the conventional systems driven by electricity. Solar-driven absorption refrigeration technology has the potential to reduce the peak electricity demand and the global warming. A binary fluid, Lithium Bromide (LiBr)-water, is one of the common fluids that is widely used for solar thermal air conditioning applications [1, 2]. The schematic flow diagram of a conventional absorption chillers is shown in (Fig. 1a). The absorption refrigeration process works using binary fluid of an absorbent (frequently LiBr) and a refrigerant (water) [1]. In this system, the compressor is replaced by an absorber, a solution pump and a heat source substituting the electrical power for the vapor compression. Briefly, an absorption refrigeration process which uses LiBr absorbent, operates in four key stages:

-The diluted LiBr in water is pumped from the absorber into the generator. In the generator, the solution is heated which leads to vaporize the refrigerant. Then, the vapor flows to the condenser and the concentrated LiBr solution flows to the absorber.

-The cooling water absorbs the heat of condensation from the vapor in condenser, changing the refrigerant into a liquid phase.

-The liquid water is pumped to the evaporator and expands through spraying on the top of the chilled water tubes. The pressure and temperature of refrigerant drop in during the expansion. At low pressure of evaporator, the water vaporizes and removes the energy of chilled water in tubes.

-In the last stage, the vaporized water moves from the evaporator to the absorber. In the absorber, the vapor and vapor absorption heat are adsorbed by the concentrated LiBr solution and the cooling water, respectively. Therefore, the concentrated solution returns to a diluted state which is, then, pumped to the generator to complete the refrigerant cycle.

The absorption chillers are more environmentally friendly as compared to the vapor compression systems since (i) no chlorofluorocarbons and derivatives are used in the process, (ii) moving parts are only pumps and hence operate smoothly without generating noise. Furthermore, solar thermal, biomass or another renewable source of energy can be used to drive the absorption cycle (Fig. 1b). It has been reported that by dispersing the stable nanoparticles (NPs) into the water, more solar light energy could be trapped which could further improve the system efficiency [3, 4] and the heat transfer phenomena. Therefore, the efficiency of solar air conditioner could be

increased by using a LiBr based nanofluids. It has been suggested that with appropriate modification of the system, the added NPs could improve the solar absorption leading to the increase of the separation effect and at the same time the absorption efficiency [5].

However, a number of challenges need to be solved first, and one in the forefront is the NPs stability issue. The concentration of LiBr salt differs from one design to another and varied in different parts of absorption refrigeration system that falls into a large range of 10-50 weight percent [6, 7]. Though there are plenty of works published on the topic of nanofluids and nanofluids stability, nearly all were based on a single base fluid, either water or oil. The stability of NPs in a pure fluid is relatively easy to be achieved, however for a binary fluid, especially with a high ionic component such as LiBr, it is much more difficult. The high concentration of LiBr would compress the electrical double layer (EDL) around NPs (Fig. 1b). The combined magnetic and Van-der-Waals attractive forces would dominate the electrostatic repulsion, which results in the agglomeration of NPs. There are basically two possible approaches to achieve a good dispersion and stability of NPs: particle morphology control and extra steric stabilization. Colloid chemistry suggested that when the size of particles in a fluid is smaller than a critical size, R_c, Brownian motion of NPs (diffusion) would overcome the sedimentation to form a stable dispersion [8]. In addition, the decrease of electrostatic repulsion force arising from the compression of EDL could be compensated by an effective functionalizing of NPs that promotes the steric repulsion. In addition, the photo-thermal conversion characteristic of a binary nanofluid is barely studied; albeit, a large number of publications have been reported for pure liquids [9, 10].

This work aims to evaluate the photo-thermal conversion efficiencies of long-term stable NPs dispersions into a binary fluid including high concentrations of LiBr. Iron oxide NPs is selected as a low cost and promising NPs in absorbing solar energy [11, 12]. Steric stabilization with careful selection of stabilizers is used to form stable NPs dispersions whose performance is assessed by a high-speed centrifuge method via a LUMiSizer. The photo-thermal conversion and evaporation rate analysis of the engineered NPs dispersions are investigated under a solar simulator.

Fig. 1. (a) Conventional and solar-based air conditioning, (b) compression of electrical double layer in high ionic media.

2. Experiment

2.1. Material and Characterization

Among various NPs synthesis techniques, chemical precipitation reaction inside the nanodroplets of a reverse microemulsion (RM) is a versatile method for synthesizing and functionalizing of tiny NPs simultaneously [13, 14]. Moreover, the stabilizers in the structure of RM could control the growth rate of different crystal facets of NPs, which leads to form different NPs morphologies (e.g. spheres, rods or disks) [15]. The nanoparticles were prepared based on Massart co-precipitation reaction inside RM droplets [16]. The RM consisted of cyclohexane as the continuous oil phase, sorbitane monooleate (Span 80, HLB=4.3), polyethylene glycol sorbitan monolaurate (Tween 80, HLB=15) as the surfactants, propyl alcohol as cosolvent and an aqueous solution as the dispersed phase [17]. All the mentioned components, LiBr and Citric acid were obtained from Sigma-Aldrich Ltd., in analytical grade. Different concentrations of Ferrous Chloride (0.01 and 0.05 molar) were used for NPs preparation at the room temperature and 70ºC. The concentration of other reactants was prepared based on chemical stoichiometry with Ferrous Chloride. The Sodium Hydroxide solution as the reduction agent was added drop wise to the RM for a period of 10 min and was stirred over 4 h to complete the reaction. The formed NPs were analyzed by UV-Spectrophotometer (Shimadzu, UV 1800), Transmission Electron Microscope (FEI Tecnai TF20 TEM), Dynamic Light Scattering (Malvern Zetasizer ZS) and Dispersion Analyzer Centrifuge (LUMiSizer, Lum GmbH, Berlin, Germany).The concentration of nanoparticles in nanofluids was estimated using Varian 240FS Atomic Absorption Spectrophotometry (Varian Ltd, USA).

2.2. Solar experimental setup

A simulator was used for obtaining the photo-thermal conversion characteristics of NPs in order to minimize the experimental uncertainties under direct sun light (Fig.2c). This sun simulator

provides a radiation spectrum which matches the solar spectra, and the intensity can be varied by using suitable filters. This device is certified to IEC 60904-9 2007 edition, JIS C 8912 and ASTM E 927-05 standards. All the characteristics of experimental set-up has been provided in Table 1.

Table 1. characteristics of experimental set-up.

In the experiments, the pure water or nanofluid was placed in the sample container and a Fresnel lense was used to focus the sunlight. A digital weighing scale was used to measure the evaporated mass change. In order to investigate the temperature distribution inside the sample, K-type thermocouples were used among which 6 thermocouples were put inside the solar receiver to measure the temperature gradient along the light pathway; one thermocouple was put above the surface of testing sample, and another was used to measure the ambient temperature. A data acquisition system connected to a PC was used to record the readings from thermocouples and digital weighing scale under the Lab VIEW environment. Before the experiment, the sample containers were washed carefully with the pure water of ambient temperature, and all the samples were put inside a fridge and maintained at the same starting temperature (20 ºC). During the preparation stage, all nanofluids were avoided to be exposed to the sunlight. There are other assumptions in the process of measuring and calculation of photo-thermal conversion efficiency. Assuming that the radiation from the sun simulator light source was projected on the sample suspension entirely, that is, the radiation spot was no greater than the cylindrical container. Moreover, the effect of dust and tiny particles in the air on the light source radiation was ignored. In addition, the irradiation intensity was assumed to be constant and stable during the experiments (attenuation of irradiation was ignored).

Fig.2. a) Experimental set upof solar-driven evaporation,b) testing containercontaining binary nanofluid under 10 sun solar radiation and c)schematic place of thermocouples.

2.3. Photo-thermal conversion evaluation

Three kinds of efficiencies were applied to quantify and compare the effect of NPs on the photo-thermal efficiency including sensible efficiency (η_s), latent efficiency (η_l) and loss efficiency

(η_{loss}) [18]. For solar experimental system in the current study, the sum of efficiencies is equal to one as follows:

$$\eta_s + \eta_l + \eta_{loss} = 1 \quad (1)$$

The sensible efficiency (η_s) can be calculated using Eq. (1) [19].

$$\eta_s = \frac{(c_w m_w + c_n m_n)\Delta T}{IA\Delta t} \quad (2)$$

where c_w and c_n are the specific heat of water and the nanoparticles (J/g.°C); m_w and m_n are the mass of water and the nanoparticles respectively (g); I is the radiation intensity (w/m^2); and A is the illumination area of the sample (m^2); Δt is the time interval (s); ΔT is the temperature rise of sample suspension in the Δt time interval (°C). The photo-thermal conversion efficiency is proportional to the average value of temperature change and therefore the temperature is calculated based on the average of 6 different measure points. The temperature difference between the nanoparticles and the base fluid (here water) is negligible for low intensity continuous radiation and the nanoparticles mass is negligible compared to the water mass [20]. Therefore, Eq. (2) can be re-written as:

$$\eta_s = \frac{(c_w m_w + c_n m_n)\Delta T}{IA\Delta t} \approx \frac{c_w m_w}{IA} . \frac{\Delta T}{\Delta t} \quad (3)$$

The latent efficiency (η_l) was used to calculate the ratio of vaporization heat to the total radiation as follow [21]:

$$\eta_l = \frac{P_{steam}}{IA\Delta t} = \frac{r_w \Delta m_s}{IA\Delta t} \quad (4)$$

$$IA\Delta t = 10 \times 10^3 (\mathrm{W/m^2}) * \pi * (1.5 \times 10^{-2} \mathrm{m})^2 \times 40 \text{ min} \times 60 \mathrm{s}$$

where P_{steam} is the amount of solar energy consumption for producing steam, r_w is the evaporative latent heat of water and Δm_s is the vaporized mass loss during the period of Δt.

The physical and thermal properties such as density and specific heat of the nanofluid are calculated using different Eq. 5 and 6 at the mean bulk temperature [22].

$$\rho_{nf} = \phi.\rho_n + (1-\phi).\rho_w \quad (5)$$

$$c_{nf} = \frac{\phi.(\rho_{NP}c_n) + (1-\phi).(\rho_w c_w)}{\rho_{nf}} \quad (6)$$

where ρ is density (g/ml) and ϕ is nanoparticle volume fraction.

3. Results and Discussion

3.1. Binary nanofluid preparation and characterization

Fig.3a illustrates the procedure of preparation and functionalizing of iron oxide NPs. The following steps have been applied after the formation of NPs inside RM:

-Organic and aqueous phase separation were done by destabilizing the RM via addition of extra pure water. In this stage, NPs remains inside the organic phase since the tail of stabilizer molecules are hydrophobic/oiliphilic. In fact, the NPs surface was covered with a single layer of stabilizer molecules so that the tail of stabilizer is free in organic phase.

-Phase transformation of NPs from organic phase to aqueous phase was performed by the formation of double layer stabilizer molecules (admicelles) around NPs. After modification of NPs functionalization, the hydrophilic head of stabilizer molecules is free inside the aqueous phase that results in switching of hydrophobic NPs to hydrophilic one [23]. The hydrodynamic average size of NPs, before and after phase transformation, confirmed the formation of stabilizer admicelles around particles. The average hydrodynamic size of NPs was obtained equal to 7.31±0.35 nm and 11.5±0.98 nm before and after phase transformation, respectively. Around 4.6 nm increment in hydrodynamic size is an evidence for the formation of admicelles around the NPs. Fig. 3b and c illustrate the TEM images of NPs and mechanisms of rod shape appearance, respectively. The TEM images disclose the conversion of spherical morphology to rod shape by increasing the temperature and reactants concentration. Attachment of stabilizer molecules on the surface of primary nuclei, change of crystal facet growth rate (Fig. 4c) and stretching of spherical droplets of RM to ellipsoidal shape across the shear rate direction (Fig. 4c) could be the main reasons for rod shape morphology appearance [24]. Table 2 provides further information about the concentration and morphology of the final iron oxide NPs.

Fig. 3. The procedure of preparation and functionalizing of iron oxide NPs, (b) effect of temperature and reactant concentration on the morphology of iron oxide NPs and (c, d) mechanisms of rod NPs appearance.

Table 2. The characterization of iron oxide NPs at different conditions.

50 weight percent of LiBr was added to different amount of iron oxide nanofluids to produce a binary nanofluid of LiBr. A dispersion analyzer (LUMiSizer 6110) instrument was used to determine the stability of binary nanofluids, Fig. 4a [25]. A Near-Infrared (NIR) light source scans the sample during a high speed centrifugation and the stability of binary nanofluids were determined based on final transmission pattern of the NIR light. The binary nanofluids (0.5 ml) were filled in a polycarbonate capillary cell (Fig. 4b) and centrifuged for about 3 h (255 profile and 44 interval) at 3150 rpm (lightfactor1, 25 ºC, 870 nm NIR LED) which is equivalent to 6 months in real condition. The instability curves of different samples are shown in Fig. 4c.

The transmission curves of the binary nanofluids in Fig. 4d display a region of complete absorption, indicating a polydisperse sedimentation pattern without observing any particle-particle attachments [26]. Moreover, the thin width regions of NIR transmission pattern imply the high stability of samples for a long period of time.

Fig. 4. (a) Schematic configuration of the analytical centrifuge system LUMiSizer [20], (b) polycarbonate capillary cell containing samples after centrifugation process(c) instability profile and (d) NIR transmission pattern of binary nanofluids.

Fig. 5a, b also illustrate binary nanofluid samples and TEM photo of NPs ($FeCl_3$: 0.05 M, Tem=22 °C) after 6 months immobility that clearly verifies the long shelf-life of binary nanofluids.

Fig. 5. (a) binary nanofluid samples, (b) TEM and SAED images of NPs ($FeCl_3$: 0.05 M, Tem=22 °C) after six months immobility.

209 *3.2. Photo-thermal efficiency of binary nanofluid*

210 Fig.6 shows the UV-visible absorption spectra of the resulting nanofluids. The shift of UV
211 spectra to the right side could be due to increasing the NPs concentration. According to Fig. 6,
212 the rod shape particles have a slightly wider UV-visible adsorption spectrum, and they were used
213 for further analysis of photo-thermal conversion efficiency.

214 **Fig. 6.** UV-vis absorption spectra of iron oxide nanofluids with normalized absorbance.

215 Fig. 7 illustrates increasing of the nanofluids bulk temperature and deionized water under solar
216 radiative intensity of 10 sun (~10000 W/m^2) for 40 min during which the temperature was
217 recorded. After 40 min illumination, the solar simulator was shut down, and samples were stayed
218 for cooling down. According to Fig. 7a, the temperature of deionized water increased slowly, and
219 reached only to 52 ºC after 40 min illumination. Only 0.73 g water was evaporated during 40 min,
220 and the maximum evaporation rate reached only to 0.46 mg/s. In the first 20 min, temperature
221 inside the volume was non-uniform and the largest temperature difference was 5 ºC. That could
222 be due to the light intensity decreases along the optical depth which results in a higher absorption
223 rate at the surface of NPs. After that, temperature gradient shrinks to less than 2ºC indicating
224 higher surface evaporation rate could reduce the surface temperature increasing rate, leading to a
225 more uniform temperature profile. Addition of rod shape iron oxide NPs into water could
226 improve the temperature obviously (Fig. 7b, c). For iron oxide nanofluid with the concentration
227 of 64 and 321 mg/L, the highest temperature reached to 61 and 66 ºC after 40 min illumination
228 that is 17 and 27 percent higher than pure water, respectively. For both nanofluids, the surface
229 temperature was higher, and the mean temperature was more non-uniform compared to the pure
230 water and the non-uniformity of temperature was proportional to the NPs concentration.

231 **Fig.7.** Comparison of temperature of thermocouples, mass change, evaporation rate of binary
232 nanofluid and deionized water under 10 sun illumination: a) deionized water, b) 64 mg/L rod
233 shape, c) 321 mg/L rod shape.

234 The surface and bottom temperature of samples are more clearly illustrated in Fig. 8. According
235 to Fig. 8, the highest temperature (TC6) was elevated while the lowest temperature (TC1) was
236 decreased after increasing of particle's concentration. For instance, TC1 was obtained as 55.7 ºC
237 at t=40 min for 64 mg/L concentration of rod shape NPs, whilst it is estimated as 50.5 ºC at 321

mg/L. Higher concentration of NPs led to a high non-uniform temperature distributions and energy accumulations onto the surface, producing a localized heat at the surface of NPs that is beneficial for the steam evaporation systems.

Fig. 8. a) Bottom temperature (TC1) and b) surface temperature (TC6) of different binary nanofluids versus time under both 10 sun.

The highest evaporation rate raised to 0.80 mg/s for 321 mg/L NPs rod shape concentration, almost twice of that of deionized water (0.46 mg/s). According to radiative heat transfer process [27], more solar radiative energy will be converted to the thermal form when the concentration of NPs is increased. As mentioned before, the lower bulk temperature was observed for higher concentrations of NPs, indicating less sensible heat at the higher concentrations of NPs. The sensible heat and latent heat (energy consumed to evaporate water) have been calculated and illustrated in Fig. 9.

Fig. 9. a) Sensible heat and b) latent heat of different concentrations of NPs versus time under 10 sun.

The latent heat reached to 3800 J after 40 min light illumination for 321 mg/L NPs, but for the water, it is obtained less than 2000 J under the same condition at the same time, which means NPs absorbed more radiative energy to convert it to the latent form and evaporate water. In order to investigate the energy conversion efficiency, percentage of sensible heat and latent heat under 10 sun are presented in Fig.10.

Fig.10. Energy efficiency calculated from converted latent and sensible heat.

Fig. 10 clearly shows that iron oxide NPs increased the total energy absorption of solar radiative energy. For example, total efficiency for the pure water is 33.6%, but it is estimated as 42.8% for 64 mg/L spherical NPs. Increasing of NPs concentration will slightly increase the energy conversion efficiency, which is in agreement with the results of other researches [5, 28]. Increasing the NPs concentration will increase the latent heat efficiency significantly but increase the sensible heat efficiency slightly. This indicates that increasing the concentration of NPs will

absorb more solar energy and allocate more absorbed energy to evaporate the water. The purpose of adding NPs into solar receiver is not only to increase the photon trapping efficiency but also to evaporate more water under lower bulk temperatures.

4. Conclusions

In the recent years, solar air conditioning has been applied as a green and environmentally friendly system for temperature, humidity and distribution of air controlling. In this study, a high stable binary iron oxide nanofluid (50 wt% LiBr) was synthesized for applying in solar absorption air conditioning purpose.

-Uniform spherical and rod shape NPs were produced by RM method. The particles obtained with lower concentrations of NPs were small, spherical and monodispersed, whilst the NPs were converted to rod shape by increasing the concentration.

-Phase transformation method is used to engineer the stability of the nanofluid by the formation of a double layer of stabilizer molecules around the NPs. The stability analysis of NPs in the presence of 50 wt. % of LiBr confirmed obtaining the long-term stability of final nanofluid (beyond 6months).

-The analysis of bulk temperature increase and surface evaporation rate of iron oxide based nanofluids under solar simulator highlights their efficient photo-to-thermal energy conversion and the consequently enhanced vaporizing ability. Both sensible heat and latent heat capture were boosted for nanofluid, while the increasing rate of latent heat was higher than that of sensible heat by increasing the NPs concentration.

-Superior stability of binary nanofluid against the agglomeration and proper photo-to-thermal energy conversion efficacy support the use of proposed novel binary nanofluid in solar vapor adsorption refrigeration systems.

References

[1] R.J. Dossat, T.J. Horan, Principles of Refrigeration Paperback, 5 edition, Prentice Hall, 2001.

[2] A. Elsafty, Solar Air Conditioning System: Water/Lithium Bromide Vapour Absorption system Perfect Paperback, Lap Lambert Academic Publishing, 2013.

[3] O. Neumann, A. S. Urban, J. Day, Surbhi Lal, P. Nordlander, N. J. Halas, Solar Vapor Generation Enabled by Nanoparticles, ACS Nano. 7 (2013) 42-49.

[4] Q. Jiang, W. Zeng, C. Zhang, Z. Meng, J. Wu, Q. Zhu, D. Wu, H. Zhu, Broadband absorption and enhanced photothermal conversion property of octopod-like Ag@Ag_2S core@shell structures with gradually varying shell thickness, Scientific Reports, 7 (2017) 17782.

[5] A. Zeiny,H. Jin,G. Lin,P. Song,D. Wen, Solar evaporation via nanofluids: A comparative study, Renew. Energ. 122 (2018) 443-454.

[6] I.W. Eames, A LiBr-H_2O Absorption Refrigerator Incorporating a Thermally Activated Solution Pumping Mechanism, Entropy. 19 (2017) 1-14.

[7] J.Y. Jung, E.S. Kim, Y. Nam, Y.T. Kang, The study on the critical heat flux and pool boiling heat transfer coefficient of binary nanofluids (H_2O/LiBr + Al_2O_3), Int. J. Refrig. 36 (2013) 1056-1061.

[8] D. Wu, H. Zhu, L. Wang, L. Liua, Critical issues in nanofluids preparation, characterization and thermal conductivity, Curr. Nano. sci. 5 (2009) 103-112.

[9] Y. Xu, Y. Qin, S. Palchoudhury, Y. Bao, Water-Soluble Iron Oxide Nanoparticles with High Stability and Selective Surface Functionality, Langmuir. 27 (2011) 8990-8997.

[10] H.J. Kim, I.C. Bang, and J. Onoe, Characteristic stability of bare Au-water nanofluids fabricated by pulsed laser ablation in liquids, Opt. Lasers Eng. 47 (2009) 532-538.

[11] S. Khashan, S. Dagher, S. Al Omari, N. Tit, E. Elnajjar, B. Mathew, A. Hilal-Alnaqbi, Photo-thermal characteristics of water-based Fe_3O_4@SiO_2 nanofluid for solar-thermal applications, Mater. Res. Express. 4 (2017) 055701.

[12] S.C. Alfaro, S. Lafon, J.L. Rajot, P. Formenti, A. Gaudichet, Iron oxides and light absorption by pure desert dust: An experimental study, J. Geophys. Res. 109 (2004) 1-9.

[13] B. Richard, J.L. Lemyre, A.M. Ritcey, Nanoparticle Size Control in Microemulsion Synthesis, Langmuir. 33 (2017) 4748-4757.

[14] C. Okoli, M. Sanchez-Dominguez, M. Boutonnet, S. Jaras, C. Civera, C. Solans, G.R. Kuttuva,Comparison and Functionalization Study of Microemulsion-Prepared Magnetic Iron Oxide Nanoparticles, Langmuir. 28 (2012) 8479−8485

[15] A.K. Ganguli, A. Ganguly, S. Vaidya, Microemulsion-based synthesis of nanocrystalline materials, Chem. Soc. Rev. 39 (2010) 474-485.

[16] S. Laurent, D. Forge, M. Port, A. Roch, C. Robic, L.V. Elst, Robert, N. Muller, Magnetic iron oxide nanoparticles: synthesis, stabilization, vectorization, physicochemical characterizations, and biological applications, Chem Rev. 108 (2008) 2064-2110.

[17] E. Nourafkan, H. Gao, Z. Hu, D. Wen, Formulation optimization of reversemicroemulsions using design of experiments fornanoparticles synthesis, Chem. Eng. Res.Des. 125 (2017) 367-384.

[18] A. Guo, Y. Fu, G. Wang, X. Wang, Diameter effect of gold nanoparticles on photothermal conversion for solar steam generation, RSC Adv. 7 (2017) 4815-4824.

[19] H. Zhang, H. Chen, X. Du and D. Wen, Photothermal conversion characteristics of gold nanoparticle dispersions, Sol. Energy. 100 (2014)141-147.

[20] P. Keblinski, D.G. Cahill, A. Bodapati, C.R. Sullivan, T.A. Taton, Limits of localized heating by electromagnetically excited nanoparticles, J. Appl. Phys. 100 (2006) 054305.

[21] H. Jin, G. Lin, L. Bai, A. Zeiny, D. Wen, Steam generation in a nanoparticle-based solar receiver, Nano Energy. 28(2016)397-406.

[22] E. Nourafkan, G. Karimi, J. Moradgholi, Experimental Study of Laminar Convective Heat Transfer and Pressure Drop of Cuprous Oxide/Water Nanofluid Inside a Circular Tube, Exp. Heat Trans. 28 (2015) 58-68.

[23] J. Yang, J. Y. Lee, J.Y. Ying, Phase transfer and its applications in nanotechnology, Chem. Soc. Rev. 40 (2011) 1672-1696.

[24] X. Li, W. Zheng, G. He, R. Zhao, D. Liu, Morphology Control of TiO_2 Nanoparticle in Microemulsion and Its Photocatalytic Property, ACS Sustainable Chem. Eng. 2 (2014) 288-295.

[25] J. Gross-Rother,N. Herrmann,M. Blech,S.R. Pinnapireddy,P. Garidel,U.Bakowsky, The application of STEP-technology® for particle and protein dispersion detection studies in biopharmaceutical research, Int. J. Pharm. 543 (2018) 257-268.

[26] J.Gross-Rother,N. Herrmann, M. Blech,S.R. Pinnapireddy,P. Garidel,U. Bakowsky, The application of STEP-technology® for particle and protein dispersion detection studies in biopharmaceutical research, Int. J. Pharm. 543 (2018) 257-268.

[27] M.F. Modest, Radiative Heat Transfer, Second Edition, Academic Press, 2003.

[28] E.P. Bandarra Filho, O.S.H. Mendoza, C.L.L. Beicker, A. Menezes, D. Wen, Experimental investigation of a silver nanoparticle-based direct absorption solar thermal system, Energy Convers. Manag. 84 (2014) 261-267.

Table 1. characteristics of experimental set-up.

Sun simulator model	ORIEL^{R} Sol3A^{TM} Class AAA solar simulator (Newport)
Fresnel lense type	5 inches Diameter, eo^{R} Edmund optics, 30 cm focal distance
Digital balance type and accuracy	DV114C Ohaus, 4 digits accuracy
Thermocouple number, type, precision and distance from each other	8, Omega TT-T-40-SLE, precision of ±0.5°C, 3 mm
Sample container dimension	Cylindrical vessel with 30 mm diameter and 40 mm height
Distance of sun simulator light source from top of Fresnel lense	30 cm
Distance of Fresnel lense from top of sample	30 cm
Wight of sample inside digital balance	20 ml of pure water or nanofluid

Table 2. The characterization of iron oxide NPs at different conditions.

Reaction conditions	**Morphology**	**Concentration measured by AAS (ppm)**	**TEM image processing**		
			Average size	**Polydispersity index**	**Aspect ratio of rod NPs**
$FeCl_3$: 0.01 M Tem: 22 °C	Spherical	64	2.1	0.059	1
$FeCl_3$: 0.05 M Tem: 22 °C	Spherical	298	5.4	0.029	1
$FeCl_3$: 0.01 M Tem: 70 °C	Mix Spherical/Rod	61	3.6	0.263	-
$FeCl_3$: 0.05 M Tem: 70 °C	Rod	321	7.3	0.042	2.66

(a)

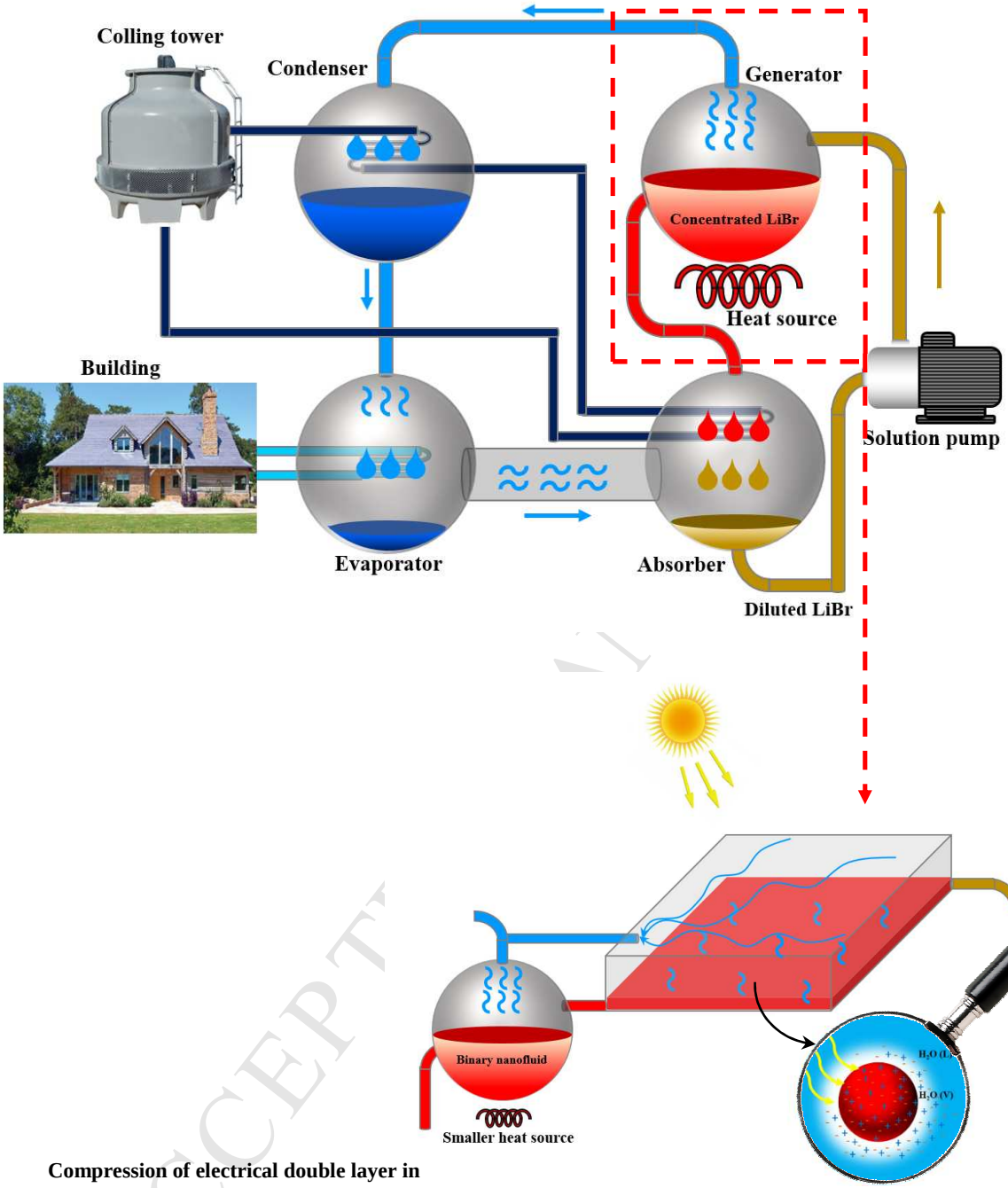
Colling tower
Condenser
Generator
Concentrated LiBr
Heat source
Building
Solution pump
Evaporator
Absorber
Diluted LiBr
Binary nanofluid
Smaller heat source
H2O (L)
H2O (V)

(b)

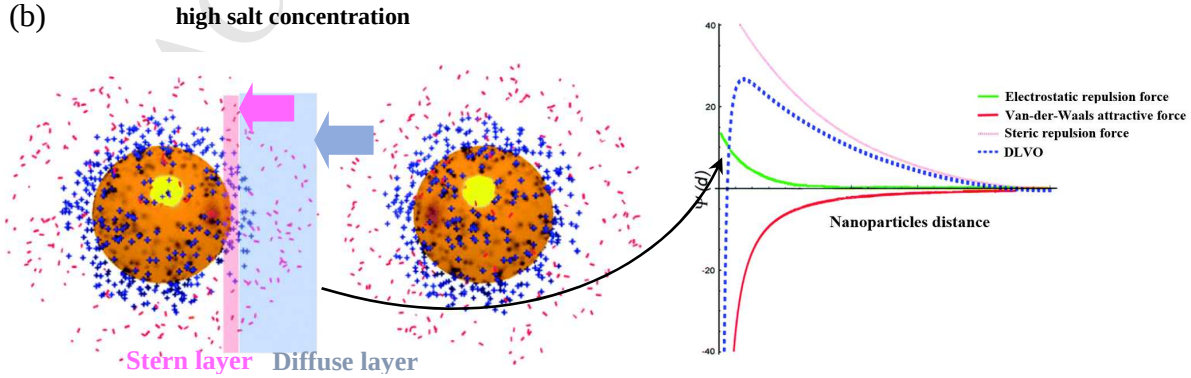
Compression of electrical double layer in high salt concentration
Stern layer
Diffuse layer
Electrostatic repulsion force
Van-der-Waals attractive force
Steric repulsion force
DLVO
Nanoparticles distance
40
20
-20
-40

Fig. 1. (a) Conventional and solar-based air conditioning, (b) compression of electrical double layer in high ionic media.

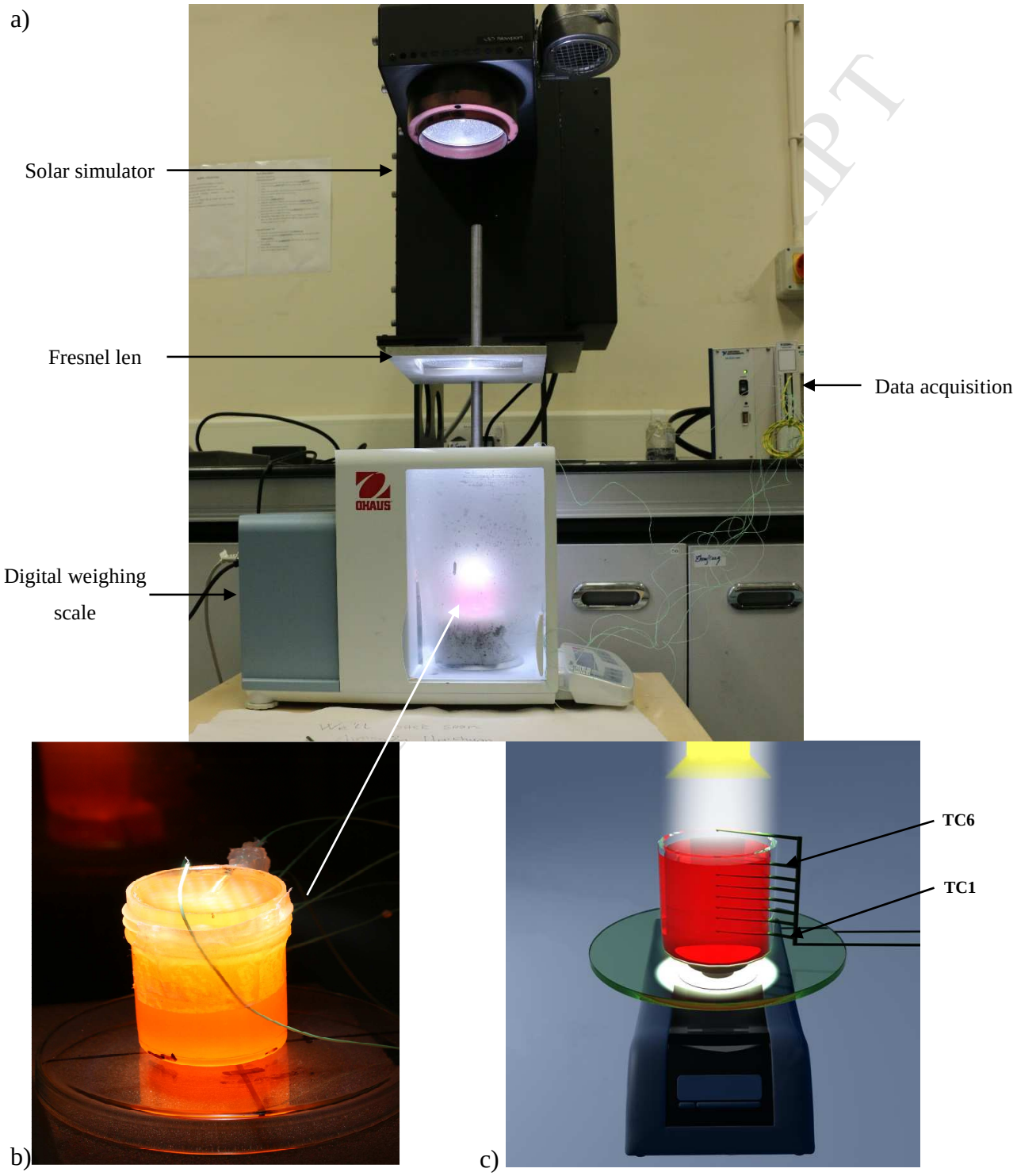

Fig. 2. a) Experimental set upof solar-driven evaporation, b) testing container containing binary nanofluid under 10 sun solar radiation and c) schematic place of thermocouples.

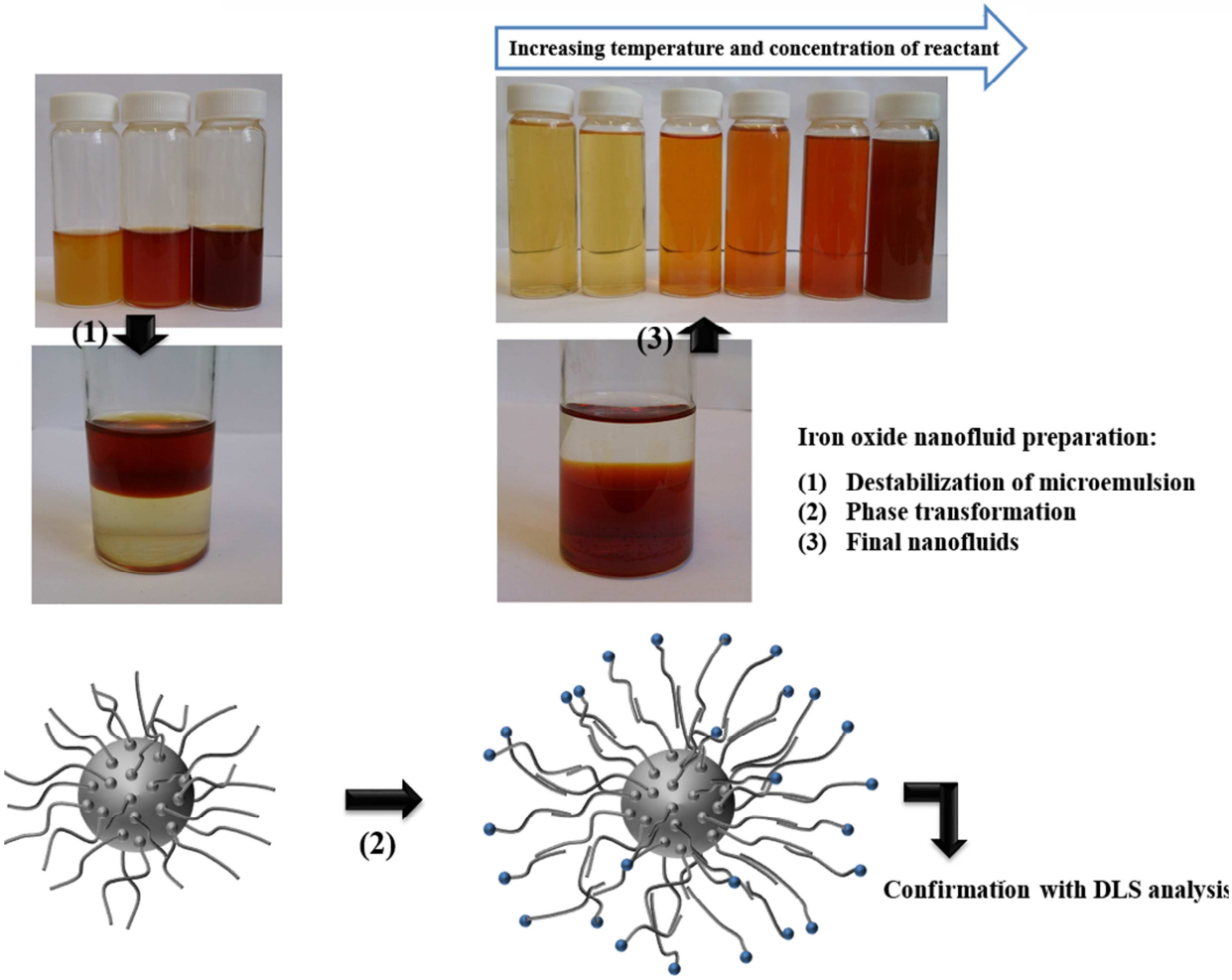
Increasing temperature and concentration of reactant
(1)
(3)
Iron oxide nanofluid preparation:
(1) Destabilization of microemulsion
(2) Phase transformation
(3) Final nanofluids
(2)
Confirmation with DLS analysis

(a)

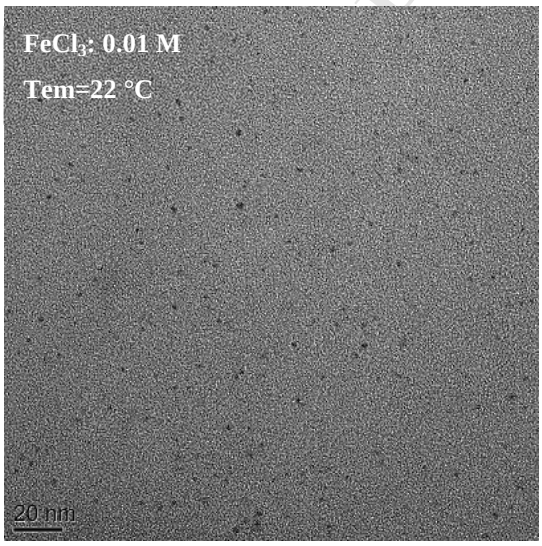
FeCl3: 0.01 M
Tem=22 °C
20 nm

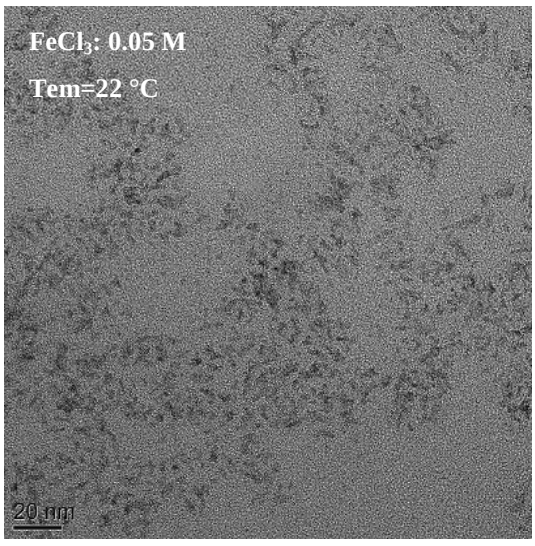
FeCl3: 0.05 M
Tem=22 °C
20 nm

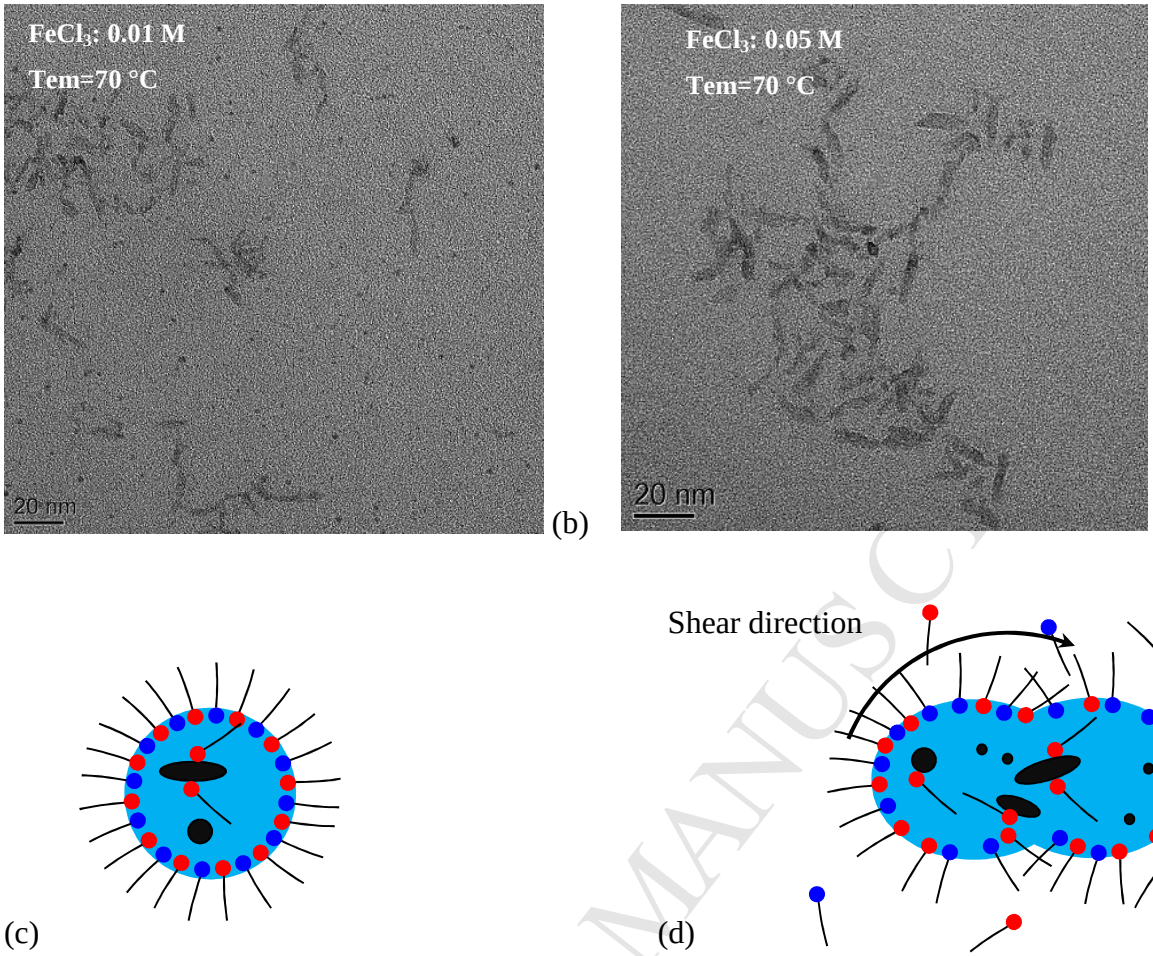

Fig. 3. The procedure of preparation and functionalizing of iron oxide NPs, (b) effect of temperature and reactant concentration on the morphology of iron oxide NPs and (c, d) mechanisms of rod NPs appearance.

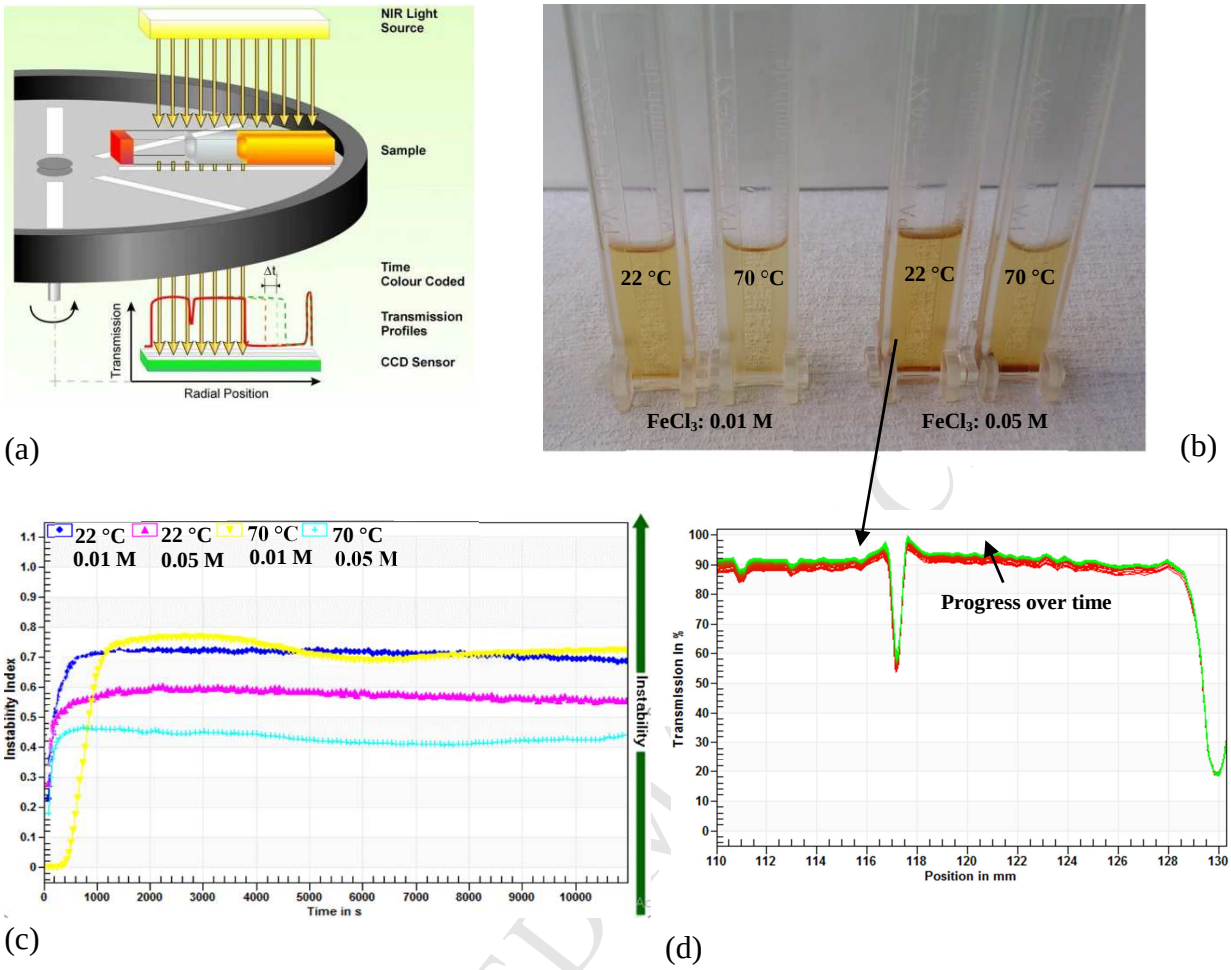

Fig. 4. (a) Schematic configuration of the analytical centrifuge system LUMiSizer [20], (b) polycarbonate capillary cell containing samples after centrifugation process(c) instability profile and (d) NIR transmission pattern of binary nanofluids.

(a)

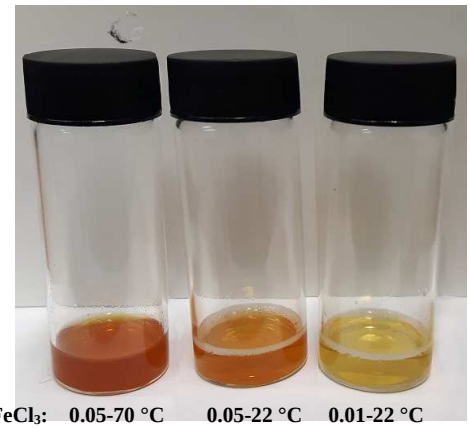

(b)

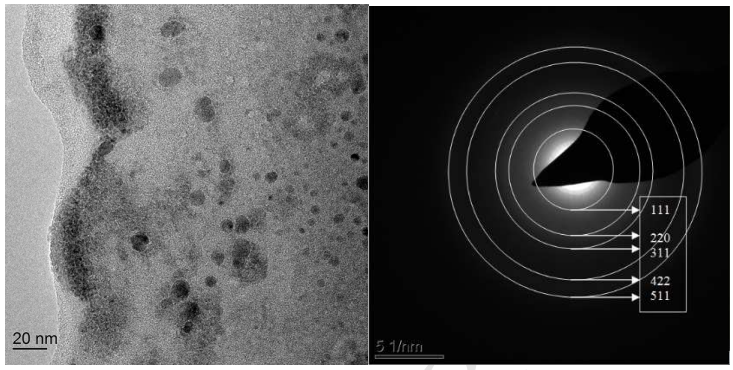

Fig. 5. (a) binary nanofluid samples, (b) TEM and SAED images of NPs ($FeCl_3$: 0.05 M, Tem=22 °C) after six months immobility.

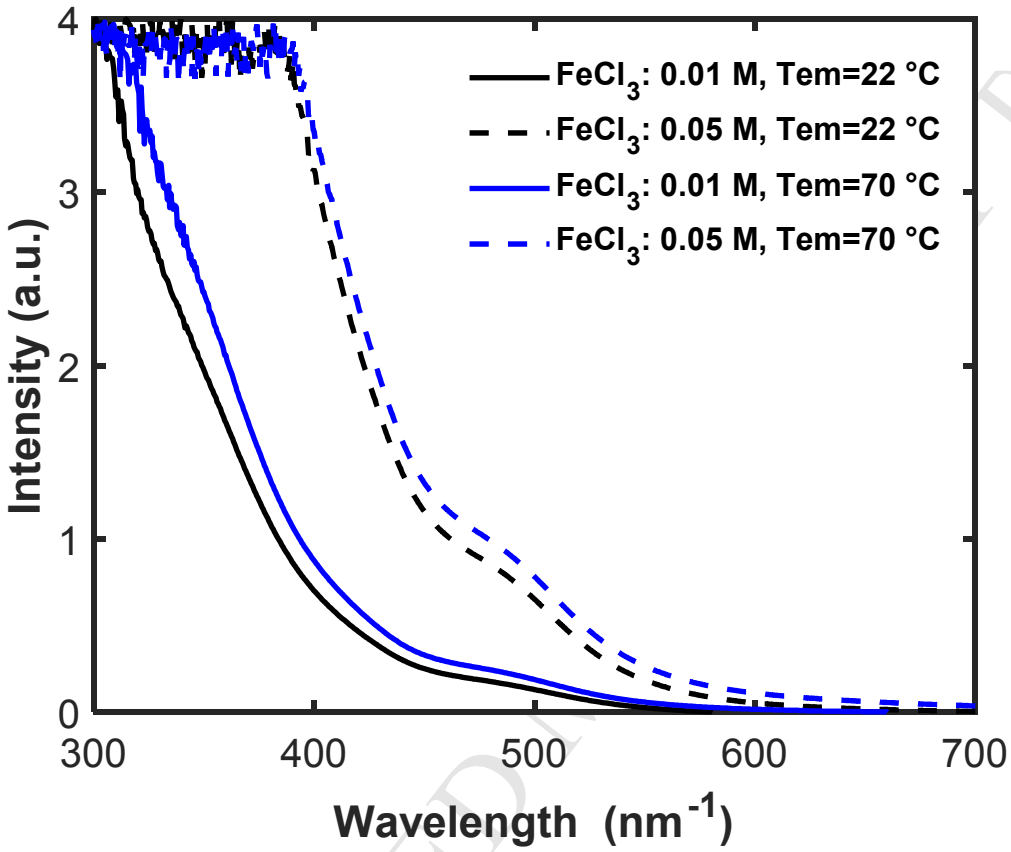

Fig. 6. UV-vis absorption spectra of iron oxide nanofluids with normalized absorbance.

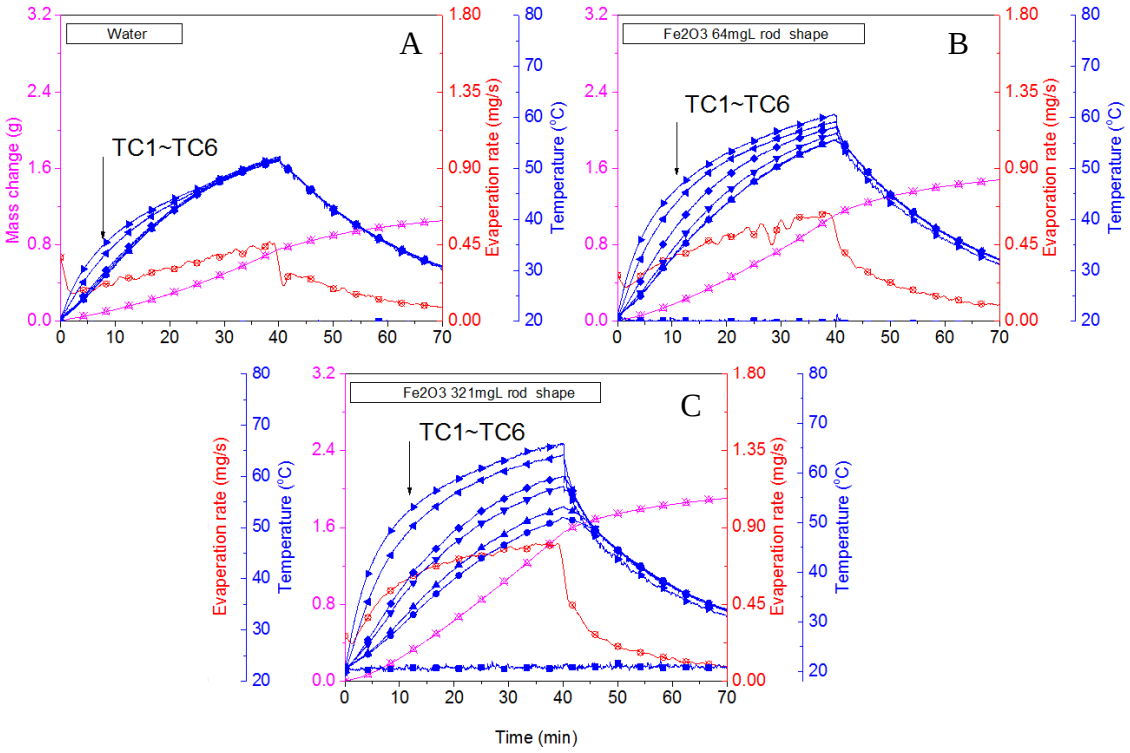

Fig.7. Comparison of temperature of thermocouples, mass change, evaporation rate of binary nanofluid and deionized water under 10 sun illumination: a) deionized water, b) 64 mg/L rod shape, c) 321 mg/L rod shape.

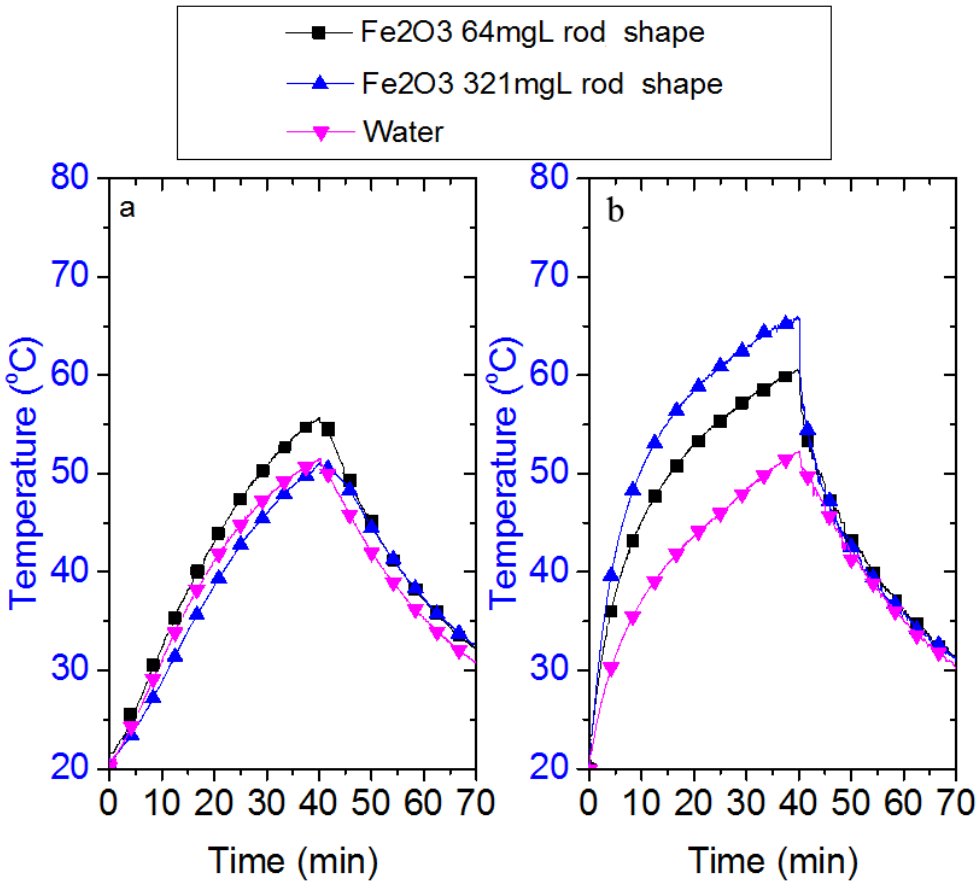

Fig. 8. a) Bottom temperature (TC1) and b) surface temperature (TC6) of different binary nanofluids versus time under both 10 sun.

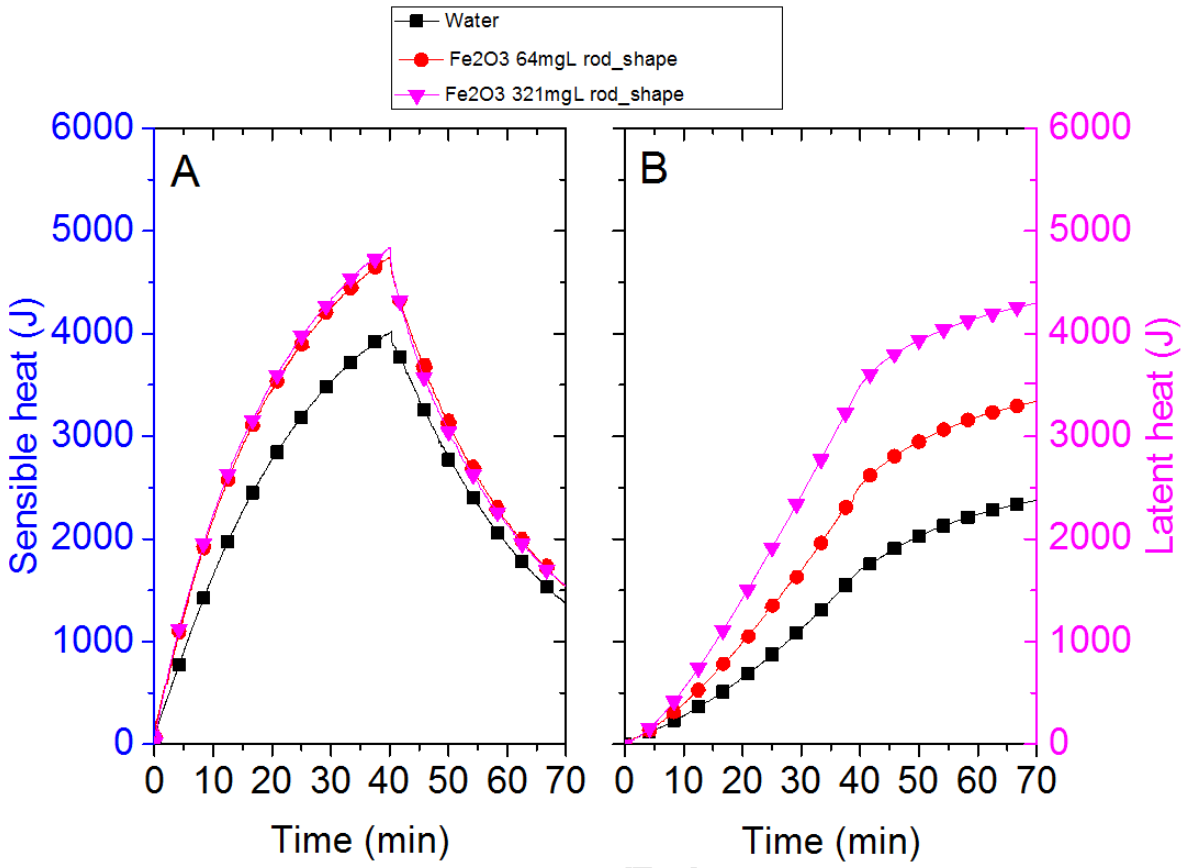

Fig. 9. a) Sensible heat and b) latent heat of different concentrations of NPs versus time under 10 sun.

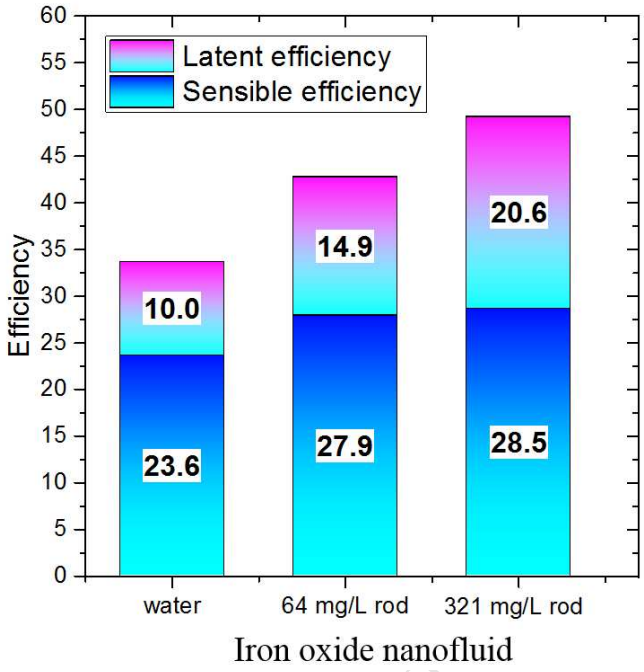

Fig.10. Energy efficiency calculated from converted latent and sensible heat.

Highlights

High stable nanoparticles have been synthesized in lithium bromide/water solution.

Photo-thermal conversion and solar evaporation properties of binary nanofluids were studied.

4.2 and 4.9% of sensible heat increasing was observed in presence of 64 and 321 mg/l of NPs, respectively.

4.9 and 11.9% of latent heat increasing was observed in presence of 64 and 321 mg/l of NPs, respectively.